Science of the Total Environment 946 (2024) 174321

Contents lists available at ScienceDirect

Science of the Total Environment

journal homepage: www.elsevier.com/locate/scitotenv

Interactions between iron and carbon in permafrost thaw ponds

Ankita Chauhan [a,b], Monique S. Patzner [a], Amrita Bhattacharyya [c], Thomas Borch [d], Stefan Fischer [e], Martin Obst [f], Laurel K. ThomasArrigo [g,h], Ruben Kretzschmar [g], Muammar Mansor [a], Casey Bryce [i], Andreas Kappler [a,b], Prachi Joshi [a,*]

[a] Geomicrobiology, Department of Geosciences, University of Tübingen, Germany
[b] Cluster of Excellence EXC 2124 Controlling Microbes to Fight Infection, Tübingen, Germany
[c] Department of Chemistry, University of San Francisco, United States
[d] Department of Soil & Crop Sciences and Department of Chemistry, Colorado State University, United States
[e] Tübingen Structural Microscopy Core Facility, University of Tübingen, Germany
[f] Experimental Biogeochemistry, BayCEER, University of Bayreuth, Germany
[g] Institute of Biogeochemistry and Pollutant Dynamics, Department of Environmental Systems Science, CHN, ETH Zürich, Switzerland
[h] Environmental Chemistry Group, Institute of Chemistry, University of Neuchâtel, Switzerland
[i] School of Earth Sciences, University of Bristol, UK

HIGHLIGHTS

- Permafrost thaw ponds have high iron (0.9–212.1 mg/L) and carbon (8.4–352.4 mg/L).
- The thaw stage of adjacent soil controls the geochemistry of thaw ponds.
- Iron in thaw ponds exists as Fe(II)-OC, Fe(III)-OC, and Fe(III)-oxide.

GRAPHICAL ABSTRACT

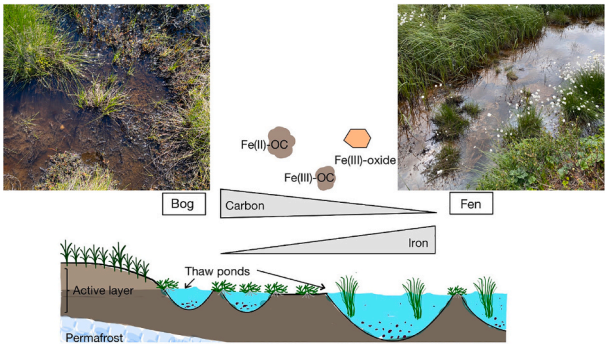

ARTICLE INFO

Editor: Shuzhen Zhang

Keywords:
Iron-carbon interactions
Iron speciation
Organic carbon
Thaw ponds
Permafrost soils

ABSTRACT

Thawing permafrost forms "thaw ponds" that accumulate and transport organic carbon (OC), redox-active iron (Fe), and other elements. Although Fe has been shown to act as a control on the microbial degradation of OC in permafrost soils, the role of iron in carbon cycling in thaw ponds remains poorly understood. Here, we investigated Fe-OC interactions in thaw ponds in partially and fully thawed soils ("bog" and "fen" thaw ponds, respectively) in a permafrost peatland complex in Abisko, Sweden, using size separation (large particulate fraction (LPF), small particulate fraction (SPF), and dissolved fraction (DF)), acid extractions, scanning electron microscopy (SEM), Fe K-edge X-ray absorption spectroscopy (XAS), and Fourier Transform Infrared (FTIR) spectroscopy. The bulk total Fe (total suspended Fe) in the bogs ranged from 135 mg/L (mean = 13 mg/L) whereas the fens exhibited higher total Fe (1.5 to 212 mg/L, mean = 30 mg/L). The concentration of bulk total OC (TOC) in the bog thaw ponds ranged from 50 to 352 mg/L (mean = 170 mg/L), higher than the TOC

* Corresponding author at: Geomicrobiology, Department of Geosciences, University of Tübingen, Schnarrenbergstrasse 94-96, D-72076 Tübingen, Germany.
E-mail address: prachi.joshi@uni-tuebingen.de (P. Joshi).

https://doi.org/10.1016/j.scitotenv.2024.174321
Received 23 April 2024; Received in revised form 24 June 2024; Accepted 24 June 2024
Available online 26 June 2024

concentration in the fen thaw ponds (8.5 to 268 mg/L, mean = 17 mg/L). The concentration of 1 M HCl-extractable Fe in the bog ponds was slightly lower than that in the fens (93 ± 1.2 and 137 ± 3.5 mg/L Fe, respectively) with Fe predominantly (>75 %) in the DF in both thaw stages. Fe K-edge XAS analysis showed that while Fe(II) was the predominant species in LPF, Fe(III) was more abundant in the DF, indicating that the stage of thawing and particle size may control Fe redox state. Furthermore, Fe(II) and Fe(III) were partially complexed with natural organic matter (NOM, 8 to 80 %) in both thaw ponds. Results of our work suggest that Fe and OC released during permafrost thaw into thaw ponds (re-)associate, potentially protecting OC from microbial decomposition while also stabilizing the redox state of Fe.

1. Introduction

Around 1700 Pg of organic carbon (OC) is stored in permafrost soils, with the top 3 m containing 70 % of this carbon (Hugelius et al., 2014; Scharlemann et al., 2014; Schuur et al., 2015; Tamocai et al., 2009). Rising temperatures in the Arctic are warming permafrost areas (Biskaborn et al., 2019), leading to their thaw, thus triggering complex feedback mechanisms that can subsequently alter global climate regimes (Turetsky et al., 2020; Walter Anthony et al., 2018). Thawing of permafrost exposes previously inaccessible carbon stocks to microbial decomposition, potentially increasing the production of the greenhouse gases like carbon dioxide (CO_2) and methane (CH_4) (Davidson and Janssens, 2006; Hodgkins et al., 2014; Harris et al., 2023). The thawing of ice underneath the soil causes the ground to collapse and leads to waterlogging, often resulting in the formation of water basins, known as "thaw ponds" (or thermokarst ponds and lakes (Pienitz et al., 2008)). These water basins are either draining or expanding depending on the hydrological conditions, which can affect the size and abundance of ponds, and their connectivity to the surrounding soil (Vonk et al., 2019). Since these thaw ponds are connected to the porewater of the surrounding soil, they may accumulate geochemical species (such as OC and different iron (Fe) species) from the thawing soil and act as biogeochemical hotspots (Vonk et al., 2015).

Depending on the formation environment and resulting geochemistry, thaw ponds may contain suspended particulate matter whose size varies along a continuum, ranging from fine particles to large-sized aggregates (Pokrovsky et al., 2016; Ogneva et al., 2023). This suspended particulate matter consists of nanometer to micrometer-sized aggregates formed by interactions between mineral particles and organic matter. Their formation can occur through abiotic processes such as the freezing and thawing of water-saturated areas, or through the aggregation of suspended particles and organic matter (Pokrovsky et al., 2018) but also biotically by the action of microorganisms and their secreted biopolymers (Fettweis and Lee, 2017). In addition, microbiological activity can transform suspended particles during thaw. These suspended particulate matter may act as elemental sinks as they can settle down after capturing nutrients, metals, microbes, and contaminants from the water column (Hirst et al., 2017; Ilina et al., 2016; Pokrovsky et al., 2016; ThomasArrigo et al., 2022; Walch et al., 2022).

Within thaw ponds, iron species may interact with OC, acting as a potential control on carbon turnover. Evidence from studies on soil from permafrost regions including Alaska, Tibet, Canada, and Sweden indicates that a significant fraction (up to 12–54 %) of total organic carbon is associated with reactive iron (Gentsch et al., 2015; Herndon et al., 2017; Monhonval et al., 2021; Mu et al., 2016; Mueller et al., 2017; Patzner et al., 2020). These associations are progressively lost over permafrost thaw, mobilizing Fe and OC from the soil. The released OC and Fe may enter the soil porewater and/or thaw ponds. Recent work has shown that thaw ponds in permafrost peatlands may contain up to 114 mg/L dissolved organic carbon (DOC; 0.45 μm filtered) and 3364 mg/L total iron (Fe_{tot}) (Pokrovsky et al., 2018), indicating the potential for re-association between Fe and C in thaw ponds, with implications for Fe and OC cycling. For example, aqueous complexes between Fe and OC (in the form of dissolved organic matter, DOM) may inhibit microbial degradation of the organic carbon (Xiao et al., 2016). In addition, the oxidation of ferrous iron (Fe(II)) may be suppressed due to complexation with DOM, leading to the persistence of Fe(II) under (sub)oxic conditions (Daugherty et al., 2017).

Emerging evidence suggests that there are interactions between Fe and OC in permafrost soils, but we know relatively little about these interactions in thaw ponds. After the thaw, the OC previously associated with iron minerals may become bioavailable. This bioavailability is likely dependent on the size fraction organic matter is present in (e.g., dissolved or suspended particulate matter) and its interaction with Fe (both Fe(II) and Fe(III)) in these size fractions. This key information, i.e., the relative distribution of iron and carbon in different size fractions (dissolved relative to suspended particulate matter), the Fe speciation, and the identity of the OC in these fractions is not known. Note that in this study, we refer to "dissolved" as the fraction that passes through a 0.45 μm pore size filter, thus also including colloids. Further, the morphology of particulate matter in thaw ponds and the spatial distribution of iron and carbon within particulate matter is not well understood. These knowledge gaps limit our understanding of coupled iron and carbon cycling in these systems. This knowledge is particularly important given that these systems may undergo redox fluctuations depending on the thaw stage, thus contributing to Fe and/or OC cycling.

In this study, we characterize the speciation of Fe and OC as well as possible Fe-OC interactions as a function of the thaw stage in pond water from a permafrost peatland complex in Abisko, northern Sweden. The peatland complex exhibits a thaw gradient, with distinct thaw stages, i.e., intact permafrost soil (referred to as "palsa"), partially thawed permafrost soil dominated by *sphagnum* mosses ("bogs"), and fully thawed soils where groundwater infiltration leads to a fen-like, sedge-dominated wetland, hereafter referred to as "fens" (Fig. 1A). We hypothesize that thawing permafrost leads to the release of previously inaccessible OC and Fe into thaw ponds, resulting in dynamic Fe-OC interactions that significantly influence carbon cycling and greenhouse gas emissions. Specifically, we hypothesize that:

1. Thaw ponds in permafrost peatland areas contain high concentrations of Fe and OC whose distribution differs based on the size fraction.
2. The accumulation of Fe and C results in the complexation of carbon by iron.
3. Reducing or redox fluctuating conditions in these thaw ponds result in mixed redox states of Fe.

The bulk samples (pond water containing suspended particles) from representative ponds were separated by size and analyzed for their elemental composition, morphology via light and electron microscopy, Fe oxidation states, and mineralogy by X-ray diffraction (XRD) and Fe K-edge X-ray absorption spectroscopy (XAS), spatial correlation between iron and carbon using scanning transmission X-ray microscopy (STXM) and functional group composition of OC by Fourier Transform Infrared (FTIR) spectroscopy. The results of this work provide a better understanding of the chemistry of Fe and OC in different fractions present in thaw ponds and their interactions.

2. Materials and methods

2.1. Site description

We chose the permafrost peatland Stordalen Mire located in Abisko, Sweden (68° 22′ N, 19° 03′ E) covering approx. 15 km^2 area to study thaw ponds (Fig. 1A). The study area experienced air temperatures ranging from 5 °C to 15 °C, with an average of approximately 11 °C, during the summer months of June–August in 2021. It also received low precipitation, with an average of about 1.25 mm/day during the same period (ICOS Sweden et al., 2022). On sampling days, no heavy precipitation occurred. Thaw ponds form at the edges of the collapsed palsa and in bog and fen regions with surface areas of 4–150 m^2 (Kuhn et al., 2018). We measured the depth of 20 thaw ponds. Thaw ponds in the bog were 3–20 cm deep while thaw ponds in the fen were deeper, with depths ranging from 10 to 46 cm. Some *sphagnum* mosses were present in the thaw ponds in the bog (Fig. 1B). In contrast, the dominant vegetation around the fen thaw ponds was cotton grass (*Eriophorum* spp.) (Fig. 1C). We observed loose aggregates in both types of thaw ponds. The particles within these aggregates that we collected from the bog and fen thaw stages were reddish-brown and settled almost immediately after collection (Fig. 1D). We measured the concentration of dissolved oxygen (DO) in a bog thaw pond as 0.68 mg/L (<8 % oxygen saturation) at the surface whereas in the fen areas, it decreased with depth from 4.89 mg/L at 5 cm depth (54 % oxygen saturation) to 1.47 mg/L at >20 cm depth (16 % oxygen saturation). The low levels of DO in the bog thaw ponds relative to those in fens are likely due to the high content of OC, which leads to high microbial activity, depleting oxygen. In addition, the lack of hydrological connectivity in bogs results in low oxygen input (Olefeldt and Roulet, 2012). All samples were collected in field campaigns during July (summer) 2020 and 2021 from bog and fen thaw ponds.

2.2. Bulk sampling and characterization

We collected bulk samples from 20 thaw ponds (Fig. S1; Table S1) for geochemical analysis. Here, we use the term "bulk" for samples collected without size separation directly from the thaw ponds. These shallow thaw ponds are delicate and easily disrupted. When collecting samples, any mixing and the depth of sampling can create variability. To address this, we collected bulk samples that included the water as well as the

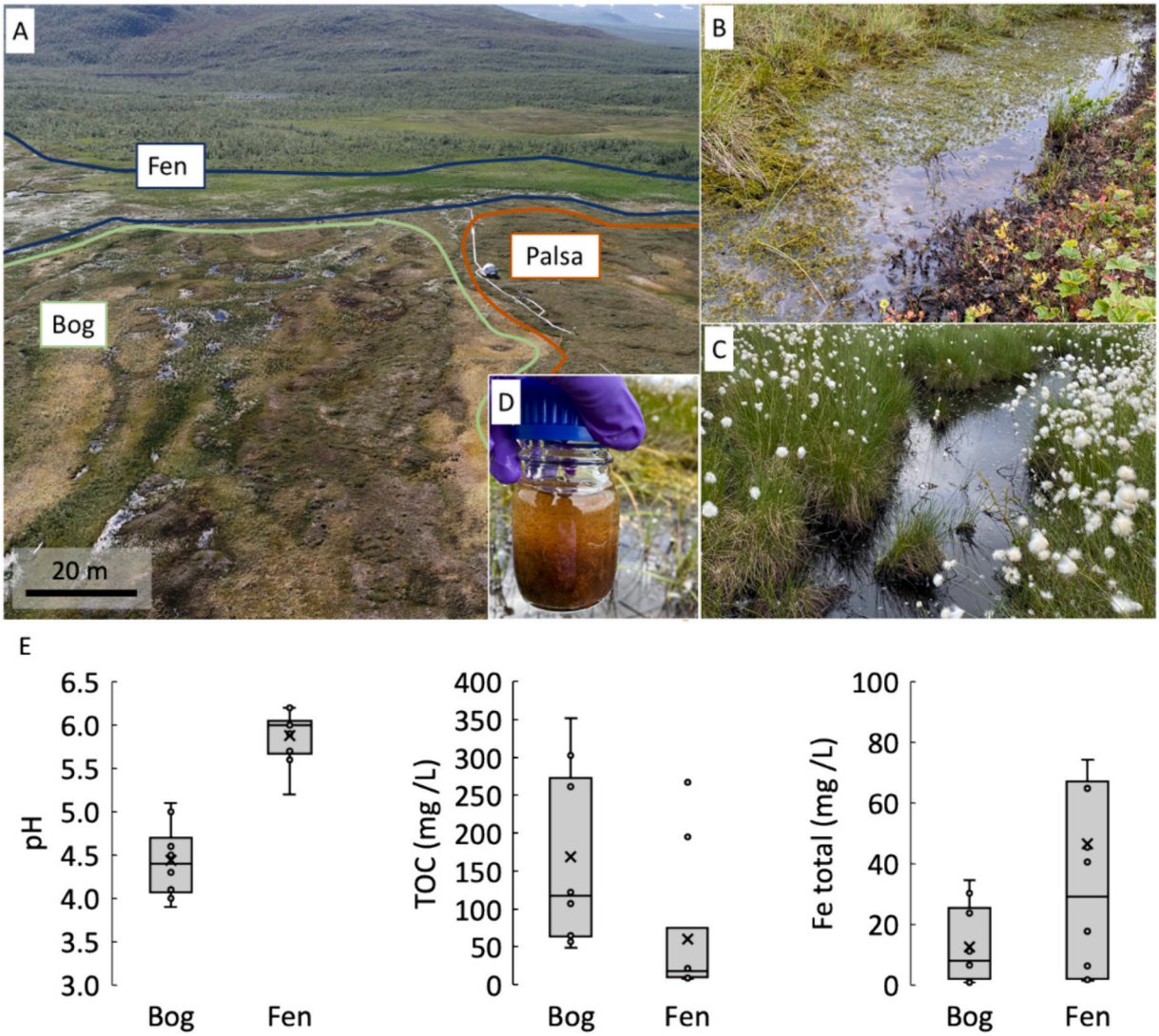

Fig. 1. Field site and geochemistry of ponds in various thaw stages. Aerial view of the field site with different thaw stages (palsa, bog, and fen) (A). Thaw pond in a partially thawed bog (B). Thaw pond within a fully thawed fen (C). Fen particles immediately after sampling (D). pH, total organic carbon (TOC), and total iron concentrations in bog and fen thaw ponds measured from 10 locations per thaw stage. The length of the box represents the interquartile range, and the whiskers symbolize the minimum and maximum values. The horizontal lines in the boxplot show the average of all values, the cross marks the median, and the circles show each data point (E).

suspended particulate matter from 20 locations in two different stages of thaw. We acknowledge that there is variability in parallel samplings from the same pond, but our primary focus is comparing the two different stages of thaw ponds (bog thaw ponds compared to fen thaw ponds). It is also important to note that when defining the particulate fraction, we must consider that this environment is not a stream or a typical lake, and therefore requires a definition specific to our system. Within this definition, we do not include a clear 'sediment' pool as we did not reach the non-suspended solids that formed the bottom of these thaw ponds. We mixed the ponds gently and collected the water with suspended particles in Schott® bottles, which were then sealed with sterilized butyl rubber stoppers. After sampling, we added 100 μL of the bulk sample to 400 μL of 1 M HCl to stabilize the unfiltered samples for Fe(II) and Fe total quantification. The stabilized samples were stored in the dark at 4 °C and later analyzed using the spectrophotometric assay (Stookey, 1970) after centrifugation (14,674 *g*). We stored the remaining bulk samples at 4 °C in the dark for TOC and elemental quantification. The TOC was quantified using a total organic carbon analyzer (High TOC II, Elementar, Analysensysteme GmbH, Germany), and samples were acidified with 2 M HCl (to remove inorganic carbon) before analysis. The elemental analyses (e.g., Na, K, Mn, Fe, P, and Al) were conducted using inductively coupled plasma mass spectrometry (ICP-MS) (Text S1; Fig. S2).

2.3. Size separation of bulk samples

Out of 20 ponds, we chose two thaw ponds (one from each thaw stage) for the separation of the suspended solids into size fractions in an anoxic glovebox (Mbraun Unilab Workstation, 100 % N_2, $O_2 < 5$ ppm, Germany). To ensure that no oxygen was present, we sparged the samples in Schott® bottles with sterile N_2 gas for 30 min before taking them inside the glovebox. The samples were sparged at a low flow rate to minimize particle breakage. Inside the glovebox, the sample was first separated by filtration (<450 μm) to remove large particles, insects, or broken large plant debris. Then, it was further divided into three operationally defined fractions: Large particulate fraction (LPF), small particulate fraction (SPF), and dissolved fraction (DF). We defined the LPF as the fraction that settled after 1 h in a 1 L bottle and contained the majority of particles on a volume basis upon visual observation. The overlying suspension was filtered using a 0.45 μm size membrane (MF-Millipore™ Membrane Filter, mixed cellulose ester (MCE)). The residue on the filter was defined as SPF and the filtrate was defined as DF (schematic in Fig. S3). The approximate size range for the fractions was calculated using Stoke's Law, as mentioned in the SI (Text S5). The particle radius cut-off range for the LPF was 2.84 μm to 70.28 μm (mean particle size measured by light scattering; Text S4; Fig. S12), and for the small particulate fraction (SPF), it was 0.45 μm to 2.84 μm. The obtained size fractions were freeze-dried anoxically (Martin Christ Alpha 1–4 LSC plus, Germany) into powders for further analysis (XAS and FTIR, detailed below).

2.4. Geochemical analysis of size fractions

We quantified Fe and OC in all size fractions by extraction with anoxic 1 M HCl (1 h). We chose this extraction as it is expected to target poorly crystalline iron oxyhydroxides (Sidhu et al., 1981) and therefore release any associated OC. We acknowledge that this may be an underestimate as certain fractions of organic matter may precipitate or stabilize at such a low pH (Eaton et al., 1985). We quantified the extractable Fe and OC for the bulk (unseparated sample containing all fractions together) and for each size fraction. In the case of the bulk sample, we mixed the sample and added 1 mL of the sample into 1 mL of 1 M HCl. For the different size fractions: (a) LPF — was added into 1 mL of 1 M HCl, (b) SPF — the filter paper containing the SPF was folded and placed in a headspace vial containing 5 mL of 1 M HCl, (c) DF — 1 mL of the DF filtrate was added into 1 mL of 1 M HCl. The LPF was pipetted from the bottom of the bottle and added into the vial containing 1 M HCl. After 1 h of extraction, the samples were centrifuged at 14,674 *g* for 10 min, and the supernatants were collected for all the fractions. To account for OC from the filter, we placed an unused filter paper in 5 mL of 1 M HCl as a control. The measured OC of the filter extract was then subtracted from the sample values. The released Fe was quantified using the spectrophotometric assay and the released OC using the TOC analyzer.

2.5. Imaging via microscopy

2.5.1. Light microscopy

For the visualization of particles present within the thaw ponds, 1 mL of the bog and fen bulk samples from the anoxically stored bottles were transferred to a 1.5 mL Eppendorf tube. A subsample (6 μL) was mixed with 2 μL of the SYTO9 green fluorescent dye (LIVE/DEAD™ BacLight™ Bacterial Viability and Counting Kit, Thermo Fisher Scientific Inc., Massachusetts, USA) to stain the cells for detection of living cells using a fluorescence microscope (Leica Microsystems GmbH, Wetzlar, Germany) at 40× magnification. The samples were also viewed under a stereomicroscope for the morphological characteristics of the particles (Text S2; Fig. S4).

2.5.2. Scanning electron microscopy (SEM) and energy dispersive X-ray analysis (EDX)

SEM was done on samples from bog and fen thaw ponds. To prepare samples, 1 mL of the bulk (i.e., unseparated) sample from the Schott bottle was added to a 12-well plate, containing poly-L-lysin-coated glass slides. The particles were set to settle down and attach to the poly-L-lysin for 30 min. Avoiding any sample movements such as bubbling or centrifugation, this procedure kept the size and morphology of the particulate matter intact during chemical fixation and washing steps. Chemical fixation was performed with 2.5 % glutaraldehyde at 4 °C for 2 h. For the preparation of the fixative, we used the liquid phase of the original sample by aliquoting 1 mL of the bulk sample and centrifuging at 14,674 g for 10 min. The supernatant was used as the medium for glutaraldehyde. After fixation, the samples were washed two times with double deionized water (Barnstead MQ system, Thermo Fisher Scientific, Germany, >18 MΩ cm) and then the subsequent dehydration was done with ethanol solutions of increasing concentrations (30, 70, and 99 %, each step for 5 min) and two times with 100 % ethanol for a cycle of 30 min each. Finally, the glass slides were dipped twice in hexamethyldisilazane (HMDS) for 30 s each and then dried on filter paper in a fume hood at room temperature. The glass slides were attached using adhesive carbon tape to aluminum stubs which were then coated with 8 nm of platinum using a BAL-TEC SCD 005005 sputter coater. Image acquisition was done using a Crossbeam 550 L Focused Ion Beam SEM (Zeiss, Oberkochen, Germany) operating at an acceleration voltage of 2 kV (for the morphological characterization) and a working distance of 5 mm. All images were taken using the secondary electron secondary ion (SESI) detector. An Oxford Instrument Energy Dispersive Spectrometer (EDX) detector (UltimMax 100) and AZtecEnergy Advanced software were used in combination with manual interpretation for the EDX analysis at an acceleration voltage of 20 kV and a working distance of 5 mm. Four replicates per sample were analyzed for elemental characterization by mapping and point scans. Point scans were also done on the background for reference.

2.6. Scanning transmission (soft) X-ray microscopy (STXM)

Fen samples for STXM analysis were suspended in anoxic ultrapure water (Seralpur PRO 90C). One μL aliquots were deposited onto formvar coated 300 mesh Cu TEM-grids (Plano GmbH, Wetzlar, Germany) in a glovebox (Glovebox Systemtechnik, 100 % N_2, $O_2 < 1$ ppm), blotted, and dried immediately. The samples were analyzed at the spectromicroscopy beamline 10ID-1 at the Canadian Light Source (CLS)

(Kaznatcheev et al., 2007). The 2D image stacks of regions with several particles each were recorded across both the C-1s and the Fe-2p absorption edges. The selected energy step sizes in the energy regions of interest were 0.1 eV at the C-1s and 0.15 eV at the Fe-2p absorption edge. STXM data were processed using the aXis2000 software package (Hitchcock, 2023). The image stacks were corrected for glitches, concatenated, aligned, and converted to linear absorbance scale where the optical density (OD) is calculated according to

$$OD = -ln(I/I_0)$$

where I is the intensity and I_0 is the intensity in the empty regions adjacent to the sample region. The Fe-2p stacks were analyzed by linear decomposition using spectra of pure siderite as a model representing Fe (II), and goethite, representing Fe(III). The resulting Fe(II) and Fe(III) distribution maps were masked by thresholding and spectra of the respective Fe(II)-rich or Fe(III)-rich regions were then extracted at both the Fe-2p and the C-1s edges. The maps of Fe(II) and Fe(III) were superimposed in an RGB overlay with a C map that was derived by subtracting the average of all images in the C1s pre-edge (275–282 eV) from the average of all images in the post edge (285–340 eV). The 2D histograms of both Fe phases with C were derived after automated thresholding to exclude background noise using the Fiji plugin ScatterJ, which was also used to calculate the respective Pearson's correlation coefficients (Schindelin et al., 2012; Zeitvogel et al., 2016).

2.7. Iron K-edge X-ray absorption spectroscopy (XAS)

To determine the Fe oxidation state and speciation in our samples, Fe K-edge (7112 eV) X-ray absorption spectroscopy (XAS) was conducted on beamline 4-1 at the Stanford Synchrotron Radiation Laboratory (SSRL), at Menlo Park, CA under ring operating conditions of 3 GeV with a current of 450 mA. Anoxically freeze-dried thaw pond fractions were gently homogenized using a mortar and pestle in a glovebox (MBraun Unilab Workstation, 100 % N_2 atmosphere, Germany), mixed with polyvinylpyrrolidone (PVP), and pressed into pellets of 7 mm diameter. The pellets were fixed between Kapton® tape and kept anoxic until measurements at the beamline. Since the mass and Fe content of the SPF was very low compared to that of LPF and DF, we focused on the DF and LPF for XAS analyses. A double crystal Si (220) monochromator was used and spectra were collected at 80 K (using a liquid N_2 cryostat) in fluorescence mode with a Lytle detector. Between 6 and 8 individual spectra were averaged for each sample. Pure elemental Fe foil was used for energy calibration for Fe at 7112 eV. The fluorescence Fe X-ray absorption near edge structure (XANES) and extended X-ray absorption fine structure (EXAFS) spectra were averaged, and pre-and post-edge subtracted using Athena (Ravel and Newville, 2005). First, a linear combination fitting (LCF) was performed on normalized Fe K-edge XANES to determine the redox state of iron. The subset of references used included Fe(II)-NOM, Fe(III)-citrate, and ferrihydrite. The k^3-weighted Fe K-edge EXAFS analysis was also performed using Athena to identify potential Fe-bearing phases in the samples (Ravel and Newville, 2005). LCF of spectra was performed in k^3-weighted k-space between k = 2 and 12, using the following end-members: siderite ($FeCO_3$), 2-line and 6-line ferrihydrite ($Fe(OH)_3{\cdot}nH_2O$), goethite (α-FeOOH), ferrosmectite, Fe(II, III)-catechol, Fe(II) complexed with Suwanee River Humic and Fulvic Acids (Fe(II)-SRHA), Fe(II)-$SRNOM_{red}$ and Fe(III)-citrate. (Details of Fe(II)-NOM preparation and characterization are provided in Daugherty et al., 2017). These references were chosen based on their likelihood to be present under experimental conditions. Fe(III)-citrate and 6-line ferrihydrite are used as references in combination to represent Fe(III) species whereas Fe(II)-$SRNOM_{red}$ is used for Fe(II) species. Although a traditional uncertainty measure such as standard deviation is not possible with XAS due to sample and beamtime limitations, the low R-factor and reduced χ^2 values of the LCF fits indicate the goodness of fits. In the fitting procedure, only components contributing 5 % or more were included as smaller contributions could not be uniquely identified.

2.8. Fourier transform infrared (FTIR) spectroscopy

The organic functional groups in the size fractions from the thaw ponds were characterized by Fourier Transform Infrared (FTIR) spectroscopy (VERTEX 80v vacuum FTIR spectrometer, Bruker Optik GmbH, Germany). The anoxically freeze-dried material of each fraction (2 mg) was mixed with 248 mg of potassium bromide (KBr), homogenized using a pestle and mortar, and pressed into a pellet. The spectrometer was set up to scan from 400 to 4000 cm^{-1}, recorded with a resolution of 4 cm^{-1}. We collected and averaged 32 scans per sample. The collected spectra were baseline corrected and functional groups were assigned to the peaks observed in the spectra based on past studies (Heller et al., 2015; Hodgkins et al., 2014; Li et al., 2020; Pedersen et al., 2011; ThomasArrigo et al., 2014).

3. Results and discussion

3.1. Bulk chemical characterization of thaw ponds

We first discuss unfiltered bulk water in thaw ponds, containing both particles and dissolved fraction. A comparison of pH, TOC, and Fe concentrations in bog and fen thaw ponds will help us understand the differences and similarities between ponds at different thaw stages. The geochemistry of the thaw ponds was influenced by the vegetation and soil geochemistry in each thaw stage. The pH of the ponds in the *sphagnum*-dominated bog ranged from 3.9 to 4.5 (4.4 ± 0.4; mean ± standard deviation) and that of the fen thaw ponds ranged from 5.2 to 6.0 (5.9 ± 0.3) (Fig. 1E), consistent with previously measured porewater pH ranges at the same field site (Patzner et al., 2020). The measured TOC concentrations in the bog ponds were between 50 and 352 mg/L (mean = 170 mg/L). These values are consistent with past measurements of DOC (measured based on 0.45 μm size cutoff) from Stordalen and the neighboring Storflaket mire thaw ponds (40 to 114 mg/L; Payandi-Rolland et al., 2020; Pokrovsky et al., 2018) and higher than those reported for western Canadian permafrost lakes (14 to 63 mg/L; Kuhn et al., 2018). The TOC concentration was significantly lower in the fen thaw ponds ($p < 0.015$), ranging from 8.5 to 268 mg/L, with an average of 17 mg/L. Although we observed high TOC values (196 and 268 mg/L, respectively) for two fen thaw ponds (Fen 1 and 2, Table S1), the majority of fen thaw ponds had TOC concentrations < 50 mg/L (Fig. 1E). We speculate that Fen 1 and Fen 2 were hydrologically connected to adjoining bog areas, resulting in high TOC values (Fig. S1) and thus more likely influenced by the bog geochemistry.

Both bog and fen thaw ponds exhibited high iron concentrations. The suspended iron concentrations in bog ponds ranged from 1 to 35 mg/L with a mean of 13 mg/L. The concentrations measured in fen ponds were substantially higher: 1.5–212 mg/L, with a mean of 30 mg/L. The higher iron concentrations in the fen thaw ponds relative to the bog thaw ponds are indicative of the geochemistry of the soil bordering the thaw ponds; porewater from fen soils generally exhibits higher iron concentrations (up to 85 mg/L in fen soil compared to 45 mg/L in bog soil porewaters (Patzner et al., 2020)). Fens are connected to the groundwater, resulting in more hydrological input of inorganic chemical species and higher concentrations of cations such as Fe and Na than bogs. The iron and carbon concentrations measured here were higher than those observed in a previous study of a Stordalen thaw pond (Pokrovsky et al., 2018), likely due to (i) the filtration (<0.45 μm) of the pond water by Pokrovsky et al. or (ii) temporal or spatial heterogeneity. We observed low values of Mn (<1 % of the concentration of Fe), P (<7 % of the concentration of Fe), and Al (<4 % of the concentration of Fe) in both bog and fen thaw ponds (Fig. S2). Therefore, we expect that these elements play a minor to negligible role in our system. We chose to do bulk sample characterization for all 20 ponds and found that the differences between the thaw

stages were much more prominent than differences between thaw ponds within a specific thaw stage. For further analyses, we therefore chose smaller subsets of the samples.

3.2. Visualization of particulate matter within thaw ponds

The visualization of particles in bog and fen thaw ponds was done using microscopy. Light and stereomicroscopy showed that suspended particulate matter was heterogeneous with aggregates of different sizes (Fig. 2, and Fig. S4A, D). The aggregates were composed of decomposed plant material, minerals, and microbial cells. We used SEM to better visualize aggregate components at a smaller scale. The size of aggregates observed in the bog ranged from 100 nm up to 50 μm (Fig. S5A). The larger bog aggregates appeared to be composed of plant parts, likely *sphagnum* moss made up of hyaline cells with intact or broken membranes and larger pore spaces (Fig. S4B). The presence of visible plant debris in the large particles indicated a slow decomposition rate of peat. Bogs showed different types of organic structures as aggregates, mesh, or tubular structures (Fig. 2B, C, and Fig. S5D–F). The aggregates were more compact than those in fen thaw ponds and had a large number of encrusted, cylindrical cells (size up to 1 μm) (Fig. S5B, C).

Aggregates from fen were micron-sized, in which aggregates of smaller particles clumped together can be seen (Fig. 2F, and Fig. S6A). We speculate that these aggregates could primarily be iron oxyhydroxides, similar to reports of ferrihydrite (Fh). These are single particles of 5–6 nm packed together to form aggregates larger than 0.1 μm in diameter (Cornell and Schwertmann, 2003). We also observed ribbon-like stalks resembling structures produced by *Gallionella* spp., and encrusted *Leptothrix*-type sheaths in fen (Fig. 2E, Fig. S6B–D) (Duckworth et al., 2009), indicating possible microbial Fe(II) oxidation. Although Fe(II)-oxidizing microorganisms have not been reported in permafrost thaw ponds, Patzner et al., 2022 found abundant and active *Gallionella* spp. in collapsed palsa soils. As a comparison, the aggregates and microbial mats in Icelandic peat seepage also reported the abundance of twisted stalks of microaerophilic Fe(II)-oxidizers and *Leptothrix*-type structures (Fleming et al., 2014; ThomasArrigo et al., 2022). Different shapes and sizes of diatoms were also seen in the ponds (Fig. S4E). Additional protozoans that can be identified in bog ponds resembling the morphology of *Arcella vulgaris*, testate amoebas, and *Euglypha ciliata* which live in peat moss and aquatic plants of the forest (Fig. S4C, F) (Bobrov et al., 2002; Mieczan, 2012).

3.3. Iron and carbon chemistry of size fractions

We present Fe and OC concentrations in the fractions and the bulk (unfiltered) water in bog and fen ponds. Note that in the bulk water and the DF, particles as well as the dissolved chemical species are included. We use mg/L to express the extractable Fe and OC concentrations (normalized to the original volume of the samples collected in the field) to allow for comparison among the fractions and different thaw stages of the pond. In the bog, the extractable Fe concentration in the bulk suspension, i.e., without separation into size fractions, was 93 ± 1.47 mg/L (Fig. 3). The extractable Fe concentrations in the fractions were 0.3 ± 0.06 mg/L in LPF, 0.9 ± 0.04 mg/L in SPF, and 88 ± 3.09 mg/L in DF. The LPF had the lowest amount of Fe in the bog among all the fractions which is consistent with our observations that the bog contained large

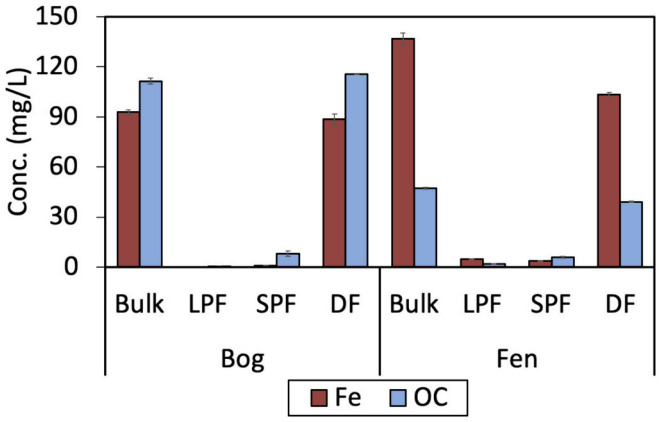

Fig. 3. Iron (Fe) and organic carbon (OC) distribution in bulk samples and different fractions. Fe and OC concentrations (conc.) based on acid extraction (1 M HCl) in bulk (i.e., unseparated) sample and different size fractions: large particulate fraction (LPF), small particulate fraction (SPF), and dissolved (DF) fraction of bog and fen. The values have been calculated back to the concentration in the original thaw pond samples. The error bars show the standard deviation between the analytical replicate measurements.

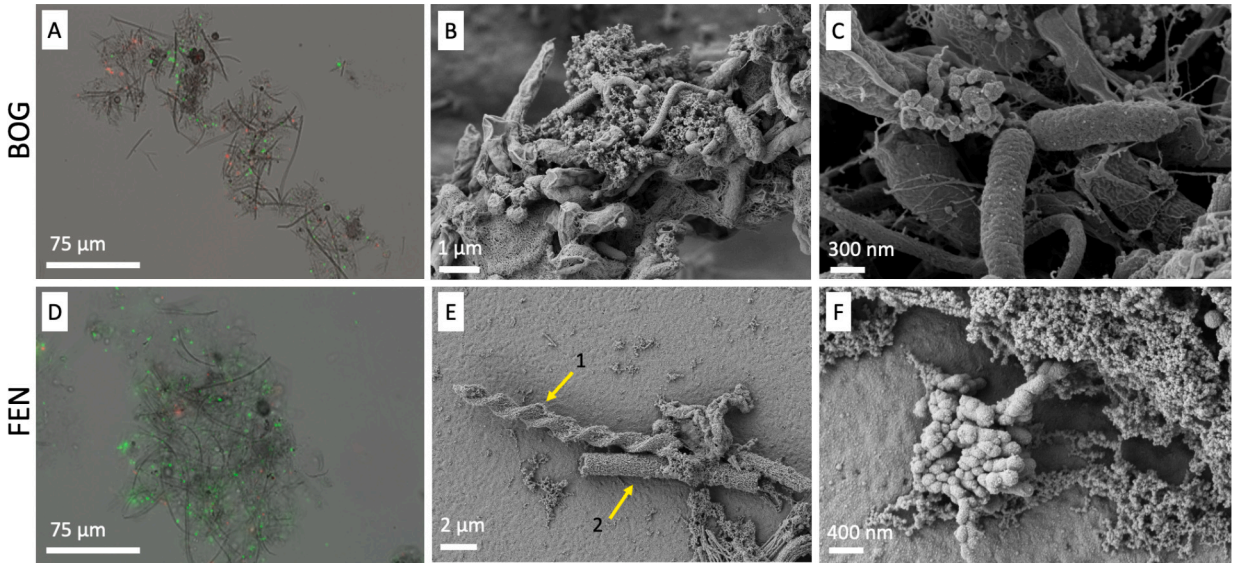

Fig. 2. Micrographs of bog and fen samples. Light microscopy (A, D) and scanning electron microscopy (B, C, E, F) images of bulk samples from bog and fen thaw ponds. In the light micrographs A and D, live cells (green), and dead cells (red) can be observed. Aggregates of minerals, microorganisms, and possible organic-rich materials in bog and fen can be seen (B, C, E, and F). The twisted stalk and sheath structures (marked with yellow arrows) are indicative of Fe(II)-oxidizing microorganisms like *Gallionella* spp.(1), and *Leptothrix*-type spp. (2) (E).

plant debris which may be present in the LPF. It is also to be noted that after the 1 M HCl extraction, the samples were centrifuged and then the extract containing the dissolved iron was measured. This could mean that the fraction of iron not extracted and dissolved by 1 M HCl is not measured for the SPF and LPF. However, we expect to have extracted most, if not all, iron by a 1 M HCl extraction based on iron speciation results below (Section 3.5). The Fe concentration in the DF was comparable to the Fe concentration in the bulk suspension, suggesting that the majority of iron in the thaw ponds was present in the DF. Such stabilization of dissolved Fe could be due to the low pH and the presence of high concentrations of OC in bog thaw ponds (Amstaetter et al., 2012; Daugherty et al., 2017). By definition, the <0.45 μm fraction contains colloids in addition to dissolved species; as a result, colloidal particles containing Fe may have been stabilized by the high OC.

As shown in Fig. 3, the bulk fen pond sample contained 137 ± 3.5 mg/L of Fe. The Fe concentrations in the bulk fen suspension were ~1.5 times higher than the concentrations in the bog. This higher concentration was likely the result of a higher water table and higher hydraulic conductivity with groundwater in the fen. An increase in the porewater Fe^{2+} concentration from palsa to fen soils has also been observed by Patzner et al. (2020). The distribution of Fe in different fen fractions showed lower concentrations in the LPF with 5 ± 0.09 mg/L and in the SPF with 4 ± 0.24 mg/L and the highest concentration in the DF with 103 ± 1.19 mg/L. Similar to the distribution of Fe in the bog thaw ponds, the majority of the Fe was present in the DF and only a small fraction was present in the SPF and LPF.

The extractable OC in the bulk suspension from the bog was 111 ± 1.80 mg/L (Fig. 3). The distribution of OC in the bog fractions was 0.60 ± 0.14 mg/L in the LPF, 8 ± 1.72 mg/L in the SPF, bulk suspension TOC, suggesting that most of the OC in bog thaw ponds is present in the DF. The total extractable OC from the bulk fen suspension was found to be 47 ± 0.64 mg/L. The OC extracted from the fen fractions was present in concentrations of 2 ± 0.16 mg/L in the LPF, 6 ± 0.48 mg/L in the SPF and, 40 ± 0.26 mg/L in the DF. The overall lower values of extractable OC in the fen fractions are consistent with the observation that the export of fen DOC is higher than the import (Olefeldt and Roulet, 2012; Tang et al., 2018). The presence of high OC in the DF is also consistent with the observation that there is high Fe in the DF, i.e., there is sufficient OC for the stabilization of dissolved Fe (Amstaetter et al., 2012; ThomasArrigo et al., 2022). The OC extracted from the bulk suspensions with acid extraction (as shown in Fig. 3) was higher than the average TOC content of the thaw ponds (as shown in Fig. 1E). This suggests the presence of OC that is likely associated with the iron minerals that were dissolved with 1 M HCl.

3.4. Spatial correlation between iron and carbon

We investigated the spatial relationship between Fe and C in the thaw pond aggregates (particles) using SEM-EDX analysis and STXM-NEXAFS (Near-Edge X-ray Absorption Fine Structure) (Fig. 4, Fig. 5, Fig. S7 and Fig. S8). SEM analysis of a representative aggregate from the bog showed that Fe amounts were low, and the main element detected was carbon (Fig. 4B). The fen showed the distribution of Fe and C throughout the aggregate structures (Fig. 4D). Iron rich hotspots were observed in which the EDX spectrum also showed C, O, Na, P, K, and Ca peaks, suggesting the presence of iron (oxyhydr)oxides and associated elements (Fig. S7). The high peaks of Si are observed due to the sample holder material. The EDX spectrum collected at a location without particles (i.e., background) indicated that the carbon signal in the aggregates was significantly higher than in the background.

Analysis of fen samples by synchrotron-based STXM-NEXAFS also showed the co-location of Fe and C (Fig. 5, and Figs. S8, S9). While SEM-EDX allowed for analyzing elemental correlations, the intrinsic NEXAFS contrast of STXM allowed for a more detailed analysis distinguishing between Fe(II) and Fe(III). Within the analyzed aggregates, Fe(II) was dominant and widely distributed all over the aggregates. In contrast, the distribution of Fe(III) was much more localized (Fig. 5C). The correlation of C with Fe(II) was very high in these aggregates with a Pearson's correlation coefficient r = 0.91 (Fig. 5D). In contrast, Pearson's correlation coefficient of C with Fe(III) was only 0.75 (Fig. S9). The strong

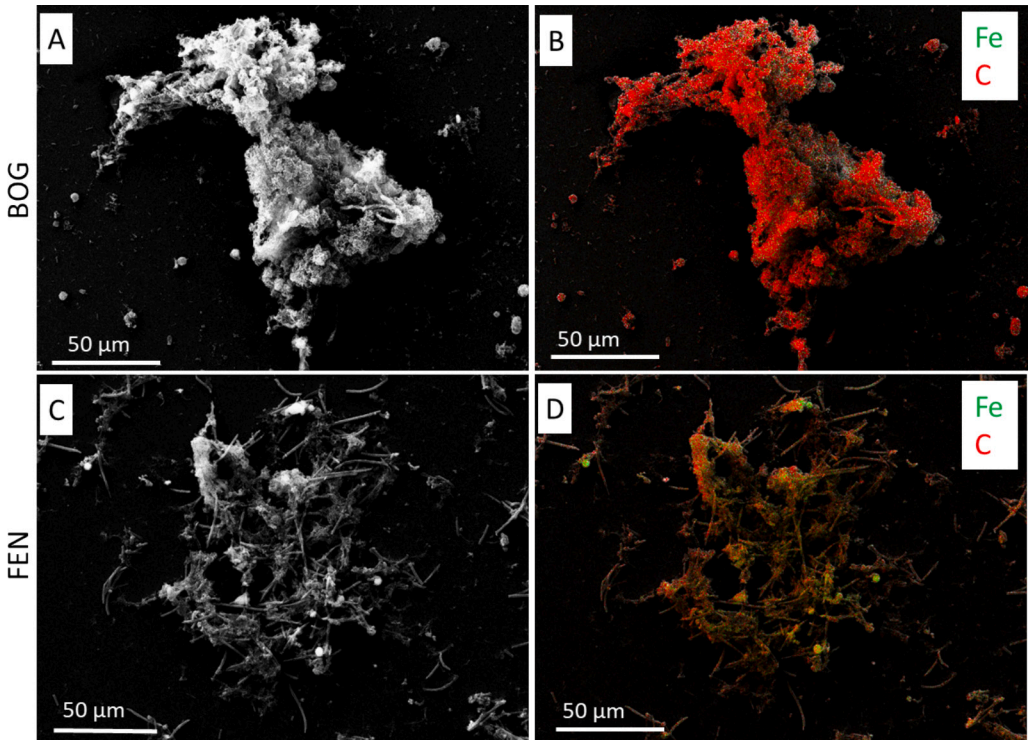

Fig. 4. Iron (Fe) and carbon (C) distribution in the particles from bog and fen thaw ponds. SEM-EDX analysis showing the distribution of Fe and C (the area highlighted by green and red respectively) in bog (A, B) and fen (C, D) aggregate.

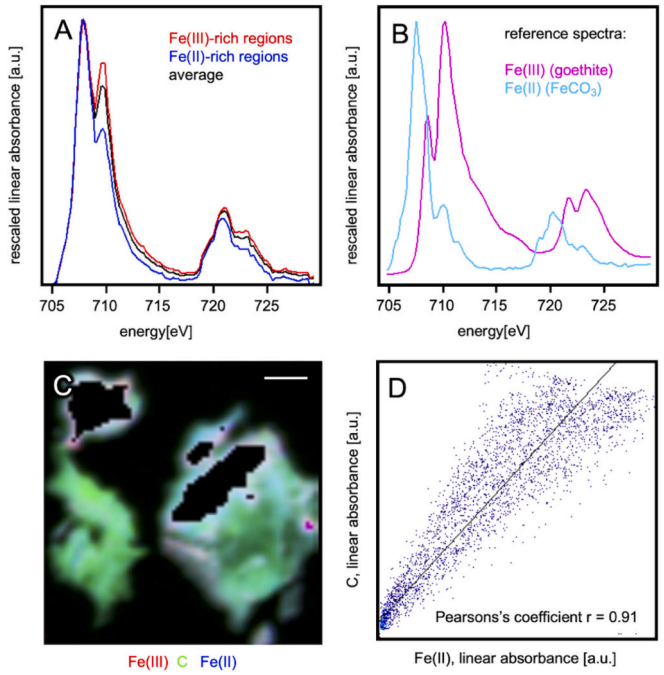

Fig. 5. Synchrotron-based STXM analysis of individual particles in fen pond samples. Rescaled Fe-2p NEXAFS spectra extracted from Fe(II) and Fe (III)-rich regions respectively of the aggregates (A). The aggregates are in general rich in Fe(II) as confirmed by spectral decomposition using spectra of known reference compounds (B). A red-green-blue (RGB) color overlay of Fe (II), C, and Fe(III) respectively, illustrates the heterogeneous distribution of the Fe species (scalebar = 1 μm). The dark regions inside the aggregates were masked for mapping to avoid problems with absorption saturation (C). The 2D histogram of the carbon (C) and Fe(II) phases illustrates a high correlation of Fe (II) with carbon, which is supported by Pearson's correlation coefficient r = 0.91 (D).

correlation of Fe(II) and C is a clear indication of a sorption or complexation process of Fe(II) with the organic carbon phase. The lower correlation of Fe(III) with carbon, the more localized distribution (Fig. 5C), and the horizontally stretched distribution at high C and Fe (III) absorbance in the 2D histogram (Fig. S8), all indicate the association of organic carbon with a precipitated Fe(III) phase.

3.5. Iron redox state and speciation in bog and fen fractions

To investigate the redox state and speciation of Fe, we used Fe K-edge X-ray absorption spectroscopy (XAS) including XANES and EXAFS regions. We analyzed the dissolved and large particulate fractions (DF and LPF) as the SPF fraction did not yield sufficient mass and was shown to contribute negligibly to the overall iron pool based on the extraction data (Fig. 3). The DF corresponds to both dissolved complexes that precipitated during freeze-drying and colloids within the <0.45 μm fraction. Based on the linear combination fitting of the XANES region, we observed the coexistence of Fe(II) and Fe(III) in all fractions (Fig. 6, Fig. S10A, and Table S2). The LPF of the bog contains 71 % Fe(II) and 29 % Fe(III) whereas DF is shown to have 53 % Fe(II) and 47 % Fe(III). Similarly, fen also displayed a distribution of Fe(II) and Fe(III) similar to the bog fractions. Fen LPF had 64 % of Fe(II) and 36 % of Fe(III), while DF had 41 % of Fe(II) and 59 % of Fe(III) (fit results shown in Table S2).

The LCF analyses of the Fe K- edge EXAFS region were performed to investigate the contribution of Fe species. The data and fit results are given in Table 1 and Fig. S10B. The LPF of the bog consisted of 62 % Fe (II)-NOM (combining Fe(II)-catechol, Fe(II)-SRHA, and Fe(II)-$SRNOM_{red}$), 27 % Fe(III)-NOM, and the rest 11 % ferrihydrite. The co-presence of Fe(II) and Fe(III) can be explained by the high

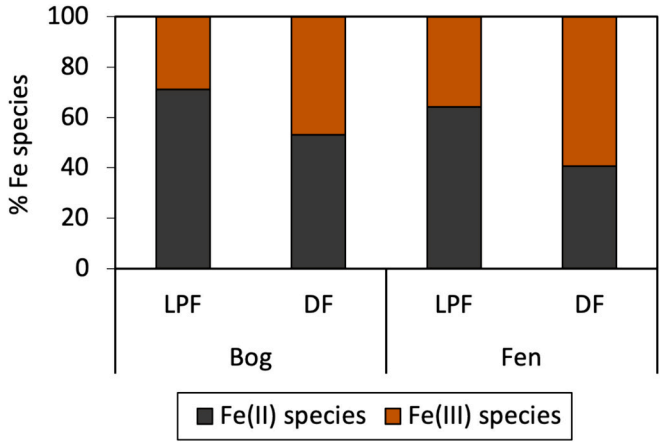

Fig. 6. Iron speciation using Fe K-edge X-ray absorption near edge structure (XANES) spectroscopy. Linear combination fitting of Fe K-edge XANES shows the iron redox state of dissolved (DF) and large particulate fractions (LPF) in bog and fen. Supplementary Table 2 contains the relative fractions in % and fit quality information.

concentrations of organic matter that complex and stabilize Fe(II) and Fe (III) at low pH. The source of dissolved Fe(II) is likely reductive iron mineral dissolution during permafrost thaw (Patzner et al., 2020). In the DF, we observed 42 % Fe(II)-NOM, 36 % Fe(III)-NOM, and 22 % poorly crystalline Fe(III) mineral ferrihydrite. Although it was initially counterintuitive that ferrihydrite, an Fe(III) mineral, was observed in the DF, one possible reason is the nanoparticulate nature of ferrihydrite. In the presence of high concentrations of organic matter, ferrihydrite nanoparticles may be stable and aggregation followed by settling may be inhibited (Amstaetter et al., 2012). As the operational definition of the dissolved fraction is <0.45 μm here, it is possible that these stabilized ferrihydrite nanoparticles passed through the filter and were present in the DF. To better understand the nature of Fe in this small size range (<0.45 μm), future work should use techniques such as ultrafiltration.

The LPF of the fen was fitted with 81 % Fe(II)-NOM, 8 % Fe(III)-NOM, and 11 % ferrihydrite. Fen DF comprised 10 % Fe(II)-NOM, 51 % Fe(III)-NOM and 39 % ferrihydrite. The presence of poorly crystalline ferrihydrite may be due to the high organic carbon concentration (40 mg C/L), similar to the bog samples. We also observed a peak in the FTIR spectrum at 791 cm^{-1} (Fig. 7), present only in fen DF. This corresponds to mineral phases (possibly H—O—Fe^{3+}) indicating the high mineral presence in the fen DF compared to the bog (Stubičan and Roy, 1961; Pedersen et al., 2011). Ferrihydrite or a ferrihydrite-like poorly crystalline phase in the fen samples was supported by the observation of weak reflections characteristic of 2-line ferrihydrite in XRD patterns (Fig. S11). In our study, X-ray absorption spectroscopy (XAS) was used to investigate the association between reactive iron minerals. Unlike traditional wet chemical extractions (e.g., dithionite-citrate-bicarbonate) that may cause redox changes, XAS allowed us to analyze the redox state of iron.

3.6. Functional group composition of organic carbon

The chemical composition of organic carbon in the dissolved and large particulate fractions (DF and LPF) was analyzed using FTIR spectroscopy (Fig. 7). Here the DF and LPF used are freeze-dried, and the DF constitutes dissolved complexes and colloids present in the <0.45 μm fraction. The data shown includes one sample from each thaw pond, which were separated into the DF and LPF fractions. Although heterogeneity exists in the ponds, we expect that our results are (qualitatively) representative given the consistency between our FTIR and STXM analyses which were done on separate pond samples. Both bog fractions exhibited a peak at 1720 cm^{-1} indicating the presence of the C═O

Table 1
Linear combination fit (LCF) results for Fe K-edge EXAFS spectra of bog and fen fraction samples.

Sample	Fe(II) species (%)			Fe(III) species (%)		R-factor	Red. χ^2
	Fe(II)-catechol	Fe(II)-SHRA	Fe(II)-SRNOM	Fe(III)-citrate	Ferrihydrite		
Bog LPF	11	46	5	27	11	0.02	0.054
Bog DF	19	0	23	36	22	0.04	0.098
Fen LPF	32	0	49	8	11	0.03	0.048
Fen DF	10	0	0	51	39	0.04	0.069

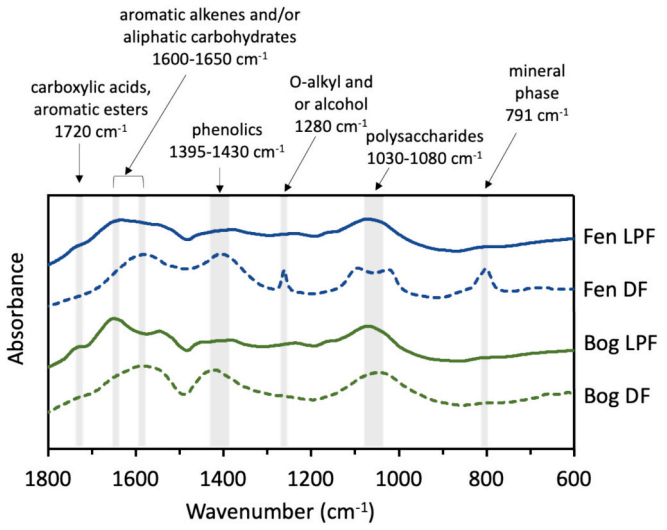

Fig. 7. FTIR spectra of separate size fractions in bog and fen. Fourier-transform infrared (FTIR) spectra of dissolved and large particulate fractions (DF and LPF) of bog and fen samples. The grey area represents the peaks characteristic of certain functional groups.

stretch of protonated carboxylic acids (COOH) or aromatic esters (Picard et al., 2019). This peak was consistent with the low pH and can be attributed to the organic acids released by *sphagnum* moss (Hodgkins et al., 2014). Additionally, peaks at 1600–1650 cm^{-1} relating to aromatic alkenes, conjugated carbonyl, or deprotonated carboxyl groups, and 1395–1430 cm^{-1} relating to COO^- or the C—O stretch of phenolic groups were observed. The DF had a distinct peak of phenolics, while the particulate fraction in bogs had a peak of aromatic alkenes. Furthermore, a peak at 1510 cm^{-1} was identified, likely corresponding to the lignin residues in the bog large particles (Mascarenhas et al., 2000). Finally, a 1030–1080 cm^{-1} peak was observed, suggesting an abundance of carbohydrates or polysaccharides in the bog ponds.

The carboxylic acid band (1720 cm^{-1}) was weaker in the fen samples, likely due to the high pH compared to the bog. The recorded peaks indicate a high level of polysaccharides (1090 cm^{-1}), with fewer lignin and aromatics (1650 cm^{-1}) relative to the bog samples, suggesting a lower abundance of aromatics in fen DF. The presence of phenolics (1430 cm^{-1}) and O-alkyl (1280 cm^{-1}) were also observed in the fen. The presence of functional groups like quinone, aromatic, phenolic, aliphatic, carboxylic, and O-alkyl in fen SPF was supported by the results of C NEXAFS analysis (Table S3), all indicating the association of organic carbon with a precipitated Fe(II) and Fe(III) phase (Fig. S9). The C NEXAFS data specifically show the association of carboxylic acids, aromatic groups, and phenol groups with both Fe(II) and Fe(III) (Fig. S9B; Table S3), consistent with past reports of Fe-organic complexation (Daugherty et al., 2017). While the NEXAFS data is based on the fen samples, we expect that similar functional groups are also involved in binding iron in the bog thaw ponds.

3.7. Implications of thaw ponds as hotspots for iron and carbon cycling

Previous studies at Stordalen Mire and other permafrost field sites have shown that Fe(III) minerals initially trap organic carbon in intact permafrost soils (Patzner et al., 2020) but thawing permafrost promotes microbial Fe(III) reduction which dissolves these minerals, releasing both carbon and iron. This undermines the stabilizing effect of iron minerals on carbon, potentially leading to the release of CO_2 and CH_4 in various thawing stages, with further microbial activity influencing this process (Hodgkins et al., 2014; Kuhn et al., 2018; Patzner et al., 2020, 2022). It is vital to determine the amount of iron and carbon in the thaw ponds because the amount of carbon in these ponds may play a significant role in greenhouse gas release.

Our research shows that thaw ponds are important systems for the interaction between iron and carbon. Thaw ponds have substantially high levels of iron and carbon, and their concentration varies in different size fractions depending on the thaw stage. Compared to fens, bogs have higher organic carbon while fens have higher iron concentrations. The Fe(II) in the thaw ponds undergoes complexation with NOM or precipitation as poorly crystalline Fe(III) (oxyhydr)oxides close to the water table, likely due to the diffusion of oxygen from the surface into the water followed by Fe(II) oxidation. These pathways thus result in Fe(II) and Fe(III) chelated by OM, as indicated by our XAS data. To our knowledge, this study has provided the first evidence of Fe-OC complexes in different size fractions ((dissolved (DF; <0.45 μm), small particulate (SPF; 0.45–2.84 μm), and large particulate (LPF; 2.84–70.23 μm)) and has shown the redox state of Fe. Since Fe-associated OC may be more protected from microbial activity (Chen et al., 2020), this might mean that the OC in the thaw ponds is similarly protected. Further, Fe (III) is stabilized in the DF, either as Fe(III)-OM or ferrihydrite, and may be stable under reducing conditions typical of anoxic periods (Mejia et al., 2018). The eventual release of organic carbon as CO_2 and CH_4 from thaw ponds is dependent on the microbial utilization of the iron and carbon. In these low oxygen systems, if Fe(III) is used as an electron acceptor, these thaw ponds may result in high CO_2 fluxes but lower CH_4 fluxes (Van Bodegom et al., 2004). Future work should focus on the understanding of the redox transformations and stability of these interactions and their contribution to CO_2 emissions from these ponds.

4. Conclusions

In this study, we investigated the biogeochemistry of iron and carbon in permafrost thaw ponds using a combination of wet chemical, spectroscopic, and microscopic techniques. Our work indicates that iron likely plays a crucial role in thaw pond geochemistry. Both bog and fen thaw ponds have significant iron concentrations (up to 100 mg Fe/L in the <0.45 μm fractions), with higher concentrations in fen ponds. The geochemistry of the surrounding soils is thought to be the cause of this variation as fen soils naturally have higher iron contents due to hydrological connectivity with the groundwater. The iron chemistry within these ponds may also be related to microbial activity based on aggregate morphologies indicative of Fe(II)-oxidizing microorganisms. Our study also showed that organic carbon is bound to iron in the form of Fe(II)-OM and Fe(III)-OM complexes based on X-ray absorption spectroscopy. This organic carbon may be less bioavailable for microbial decomposition than uncomplexed organic carbon and we speculate that

this may result in a slower release of CO_2 and CH_4. This effect should be studied further. The complexation of Fe (Fe(II) and Fe(III) species) by organic carbon, in turn, affects the stability of iron species, resulting in high Fe(III) contents in the <0.45 μm fraction. High concentrations of organic carbon may also have promoted the presence of ferrihydrite nanoparticles, a weakly crystalline Fe(III) mineral, in the DF (<0.45 μm). The Fe phases (Fe(II)-OM, Fe(III)-OM, and ferrihydrite nanoparticles) may act as electron donors and/or acceptors for Fe(III)-respiring microorganisms, thus further affecting carbon cycling within the thaw ponds.

CRediT authorship contribution statement

Ankita Chauhan: Writing – original draft, Visualization, Methodology, Investigation, Conceptualization. **Monique S. Patzner:** Writing – review & editing, Methodology, Conceptualization. **Amrita Bhattacharyya:** Writing – review & editing, Formal analysis. **Thomas Borch:** Writing – review & editing, Funding acquisition, Formal analysis. **Stefan Fischer:** Writing – review & editing, Methodology, Investigation. **Martin Obst:** Writing – review & editing, Methodology, Investigation. **Laurel K. ThomasArrigo:** Writing – review & editing, Methodology. **Ruben Kretzschmar:** Writing – review & editing. **Muammar Mansor:** Writing – review & editing, Methodology, Conceptualization. **Casey Bryce:** Writing – review & editing, Conceptualization. **Andreas Kappler:** Writing – original draft, Supervision, Methodology, Funding acquisition, Conceptualization. **Prachi Joshi:** Writing – review & editing, Supervision, Methodology, Conceptualization.

Declaration of competing interest

The authors declare that they have no known competing financial interests or personal relationships that could have appeared to influence the work reported in this paper.

Data availability

Research data will be uploaded to the FDAT Repository at the University of Tübingen.

Acknowledgments

The authors acknowledge the Abisko research station (Sweden, Abisko) especially, Jennie Wikström, Eric Lundin, Niklas Rakos, Emily Pickering Pedersen, and the Swedish Polar Research Secretariat and SITES for the support of the work done at the Abisko Scientific Research Station. SITES is supported by the Swedish Research Council's grant 4.3-2021-00164. We thank Eva Voggenreiter, Katrin Wunsch, Marie Mollenkopf, and Maike Friedel for their support in the fieldwork and assistance in the lab. We also thank Sören Drabesch for conducting the ICP-MS measurements. We are grateful to Tianran Sun and Jeremiah Shuster for their help during the SEM-EDX analysis and, also to the Tübingen Structural Microscopy Core Facility (funded by the Excellence Strategy of the German Federal and State Governments) for their support & assistance in this work. We acknowledge the support by the Deutsche Forschungsgemeinschaft (DFG, German Research Foundation; INST 37/1027-1 FUGG, AK) under Germany's Excellence Strategy, cluster of Excellence EXC2124, project ID 390838134; and support from the International Network for Terrestrial Research and Monitoring in the Arctic (INTERACT) for fieldwork support to CB. MO acknowledges the support by the DFG for the STXM measurements (Heisenberg grant OB 362/7-1 and project OB 362/4-1). Part of the research described in this paper was performed at the Canadian Light Source, a national research facility of the University of Saskatchewan, which is supported by the Canada Foundation for Innovation (CFI), the Natural Sciences and Engineering Research Council (NSERC), the National Research Council (NRC), the Canadian Institutes of Health Research (CIHR), the Government of Saskatchewan, and the University of Saskatchewan. We acknowledge the help of the spectromicroscopy beamline staff for the STXM measurements. Use of the Stanford Synchrotron Radiation LightSource, SLAC National Accelerator Laboratory, is supported by the U.S. Department of Energy, Office of Basic Energy Sciences under Contract No. DE-AC02-76SF00515.

Appendix A Supplementary data

The supporting information provides details on the distribution of Fe and C, Fe speciation, and organic functional groups present in bog and fen thaw ponds. It includes figures and tables showing the sampling locations, geochemical parameters, morphology, and elemental composition of bulk bog and fen thaw ponds. In addition, it shows SEM micrographs, XRD patterns, STXM spectra and fits, Fe K-edge XANES and EXAFS spectra, and LCF results for XANES of DF, SPF, and LPF fractions of bog and fen thaw ponds. Supplementary data to this article can be found online at https://doi.org/10.1016/j.scitotenv.2024.174321.

References

Amstaetter, K., Borch, T., Kappler, A., 2012. Influence of humic acid imposed changes of ferrihydrite aggregation on microbial Fe(III) reduction. Geochim. Cosmochim. Acta 85, 326–341. https://doi.org/10.1016/j.gca.2012.02.003.

Biskaborn, B.K., Smith, S.L., Noetzli, J., Matthes, H., Vieira, G., Streletskiy, D.A., Schoeneich, P., Romanovsky, V.E., Lewkowicz, A.G., Abramov, A., Allard, M., Boike, J., Cable, W.L., Christiansen, H.H., Delaloye, R., Diekmann, B., Drozdov, D., Etzelmüller, B., Grosse, G., Lantuit, H., 2019. Permafrost is warming at a global scale. Nat. Commun. 10 (1), 264. https://doi.org/10.1038/s41467-018-08240-4.

Bobrov, A.A., Charman, D.J., Warner, B.G., 2002. Ecology of testate amoebae from oligotrophic peatlands: specific features of polytypic and polymorphic species. Biol. Bull. 29 (6), 605–617. https://doi.org/10.1023/A:1021732412503.

Chen, C., Hall, S.J., Coward, E., Thompson, A., 2020. Iron-mediated organic matter decomposition in humid soils can counteract protection. Nat. Commun. 11 (1), 2255. https://doi.org/10.1038/s41467-020-16071-5.

Cornell, R.M., Schwertmann, U., 2003. The iron oxides: structure, properties, reactions, occurrences, and uses, Vol. 664. Wiley-vch, Weinheim.

Daugherty, E.E., Gilbert, B., Nico, P.S., Borch, T., 2017. Complexation and redox buffering of iron(II) by dissolved organic matter. Environ. Sci. Tech. 51 (19), 11096–11104. https://doi.org/10.1021/acs.est.7b03152.

Davidson, E.A., Janssens, I.A., 2006. Temperature sensitivity of soil carbon decomposition and feedbacks to climate change. Nature 440 (7081), 165–173. https://doi.org/10.1038/nature04514.

Duckworth, O.W., Holmström, S.J.M., Peña, J., Sposito, G., 2009. Biogeochemistry of iron oxidation in a circumneutral freshwater habitat. Chem. Geol. 260 (3–4), 149–158. https://doi.org/10.1016/j.chemgeo.2008.08.027.

Eaton, A.D., Clesceri, L.S., Greenberg, A.E. (Eds.), 1985. Humic Substances in Soil, Sediment, and Water: Geochemistry, Isolation and Characterization. John Wiley and Sons, New York.

Fettweis, M., Lee, B.J., 2017. Spatial and seasonal variation of biomineral suspended particulate matter properties in high-turbid nearshore and low-turbid offshore zones. Water 9 (9), 694. https://doi.org/10.3390/w9090694.

Fleming, E.J., Cetinić, I., Chan, C.S., Whitney King, D., Emerson, D., 2014. Ecological succession among iron-oxidizing bacteria. ISME J. 8 (4), 804–815. https://doi.org/10.1038/ismej.2013.197.

Gentsch, N., Mikutta, R., Shibistova, O., Wild, B., Schnecker, J., Richter, A., Urich, T., Gittel, A., Šantrůčková, H., Bárta, J., Lashchinskiy, N., Mueller, C.W., Fuß, R., Guggenberger, G., 2015. Properties and bioavailability of particulate and mineral-associated organic matter in Arctic permafrost soils, Lower Kolyma Region, Russia. Eur. J. Soil Sci. 66 (4), 722–734. https://doi.org/10.1111/ejss.12269.

Harris, L.I., Olefeldt, D., Pelletier, N., Blodau, C., Knorr, K.H., Talbot, J., Turetsky, M., 2023. Permafrost thaw causes large carbon loss in boreal peatlands while changes to peat quality are limited. Glob. Chang. Biol. 29 (19), 5720–5735. https://doi.org/10.1111/gcb.16894.

Heller, C., Ellerbrock, R.H., Roßkopf, N., Klingenfuß, C., Zeitz, J., 2015. Soil organic matter characterization of temperate peatland soil with FTIR-spectroscopy: effects of mire type and drainage intensity. Eur. J. Soil Sci. 66 (5), 847–858. https://doi.org/10.1111/ejss.12279.

Herndon, E., AlBashaireh, A., Singer, D., Roy Chowdhury, T., Gu, B., Graham, D., 2017. Influence of iron redox cycling on organo-mineral associations in Arctic tundra soil. Geochim. Cosmochim. Acta 207, 210–231. https://doi.org/10.1016/j.gca.2017.02.034.

Hirst, C., Andersson, P.S., Shaw, S., Burke, I.T., Kutscher, L., Murphy, M.J., Maximov, T., Pokrovsky, O.S., Mörth, C.M., Porcelli, D., 2017. Characterisation of Fe-bearing particles and colloids in the Lena River basin, NE Russia. Geochim. Cosmochim. Acta 213, 553–573. https://doi.org/10.1016/j.gca.2017.07.012.

Hitchcock, A.P., 2023. Analysis of X-ray images and spectra (aXis2000): a toolkit for the analysis of X-ray spectromicroscopy data. J. Electron Spectrosc. Relat. Phenom. 266, 147360 https://doi.org/10.1016/j.elspec.2023.147360.

Hodgkins, S.B., Tfaily, M.M., McCalley, C.K., Logan, T.A., Crill, P.M., Saleska, S.R., Rich, V.I., Chanton, J.P., 2014. Changes in peat chemistry associated with permafrost thaw increase greenhouse gas production. Proc. Natl. Acad. Sci. U. S. A. 111 (16), 5819–5824. https://doi.org/10.1073/pnas.1314641111.

Hugelius, G., Strauss, J., Zubrzycki, S., Harden, J.W., Schuur, E.A.G., Ping, C.L., Schirrmeister, L., Grosse, G., Michaelson, G.J., Koven, C.D., O'Donnell, J.A., Elberling, B., Mishra, U., Camill, P., Yu, Z., Palmtag, J., Kuhry, P., 2014. Estimated stocks of circumpolar permafrost carbon with quantified uncertainty ranges and identified data gaps. Biogeosciences 11 (23), 6573–6593. https://doi.org/10.5194/bg-11-6573-2014.

ICOS Sweden, Lundin, E., Rinne, J., 2022. Ecosystem meteo time series (ICOS Sweden), Abisko-Stordalen Palsa Bog, 2020-12-31–2021-12-31, Swedish National Network. https://hdl.handle.net/11676/xWk7ApA26gjb9o3hT0y98cCS.

Ilina, S.M., Lapitskiy, S.A., Alekhin, Y.V., Viers, J., Benedetti, M., Pokrovsky, O.S., 2016. Speciation, size fractionation and transport of trace elements in the continuum soil water–mire–humic lake–river–large oligotrophic lake of a Subarctic watershed. Aquat. Geochem. 22, 65–95. https://doi.org/10.1007/s10498-015-9277-8.

Kaznatcheev, K.V., Karunakaran, C., Lanke, U.D., Urquhart, S.G., Obst, M., Hitchcock, A. P., 2007. Soft X-ray spectromicroscopy beamline at the CLS: commissioning results. Nucl. Instrum. Methods Phys. Res., Sect. A 582 (1), 96–99. https://doi.org/10.1016/j.nima.2007.08.083.

Kuhn, M., Lundin, E.J., Giesler, R., Johansson, M., Karlsson, J., 2018. Emissions from thaw ponds largely offset the carbon sink of northern permafrost wetlands. Sci. Rep. 8 (1), 9535. https://doi.org/10.1038/s41598-018-27770-x.

Li, Z., Shakiba, S., Deng, N., Chen, J., Louie, S.M., Hu, Y., 2020. Natural organic matter (NOM) imparts molecular-weight-dependent steric stabilization or electrostatic destabilization to ferrihydrite nanoparticles. Environ. Sci. Technol. 54 (11), 6761–6770. https://doi.org/10.1021/acs.est.0c01189.

Mascarenhas, M., Dighton, J., Arbuckle, G.A., 2000. Characterization of plant carbohydrates and changes in leaf carbohydrate chemistry due to chemical and enzymatic degradation measured by microscopic ATR FT-IR spectroscopy. Appl. Spectrosc. 54 (5), 681–686. https://doi.org/10.1366/0003702001950166.

Mejia, J., He, S., Yang, Y., Ginder-Vogel, M., Roden, E.E., 2018. Stability of ferrihydrite–humic acid coprecipitates under iron-reducing conditions. Environ. Sci. Technol. 52 (22), 13174–13183. https://doi.org/10.1021/acs.est.8b03615.

Mieczan, T., 2012. Distributions of testate amoebae and ciliates in different types of peatlands and their contributions to the nutrient supply. Zool. Stud. 51 (1), 18–26.

Monhonval, A., Strauss, J., Mauclet, E., Hirst, C., Bemelmans, N., Grosse, G., Schirrmeister, L., Fuchs, M., Opfergelt, S., 2021. Iron redistribution upon thermokarst processes in the Yedoma domain. Front. Earth Sci. 9, 703339 https://doi.org/10.3389/feart.2021.703339.

Mu, C.C., Zhang, T.J., Zhao, Q., Guo, H., Zhong, W., Su, H., Wu, Q.B., 2016. Soil organic carbon stabilization by iron in permafrost regions of the Qinghai-Tibet Plateau. Geophys. Res. Lett. 43 (19), 10286–10294. https://doi.org/10.1002/2016GL070071.

Mueller, C.W., Hoeschen, C., Steffens, M., Buddenbaum, H., Hinkel, K., Bockheim, J.G., Kao-Kniffin, J., 2017. Microscale soil structures foster organic matter stabilization in permafrost soils. Geoderma 293, 44–53. https://doi.org/10.1016/j.geoderma.2017.01.028.

Ogneva, O., Mollenhauer, G., Juhls, B., Sanders, T., Palmtag, J., Fuchs, M., Grotheer, H., Mann, P.J., Strauss, J., 2023. Particulate organic matter in the Lena River and its delta: from the permafrost catchment to the Arctic Ocean. Biogeosciences 20 (7), 1423–1441. https://doi.org/10.5194/bg-20-1423-2023.

Olefeldt, D., Roulet, N.T., 2012. Effects of permafrost and hydrology on the composition and transport of dissolved organic carbon in a subarctic peatland complex. J. Geophys. Res. Biogeosci. 117 (1) https://doi.org/10.1029/2011JG001819.

Patzner, M.S., Mueller, C.W., Malusova, M., Baur, M., Nikeleit, V., Scholten, T., Hoeschen, C., Byrne, J.M., Borch, T., Kappler, A., Bryce, C., 2020. Iron mineral dissolution releases iron and associated organic carbon during permafrost thaw. Nat. Commun. 11 (1), 6329. https://doi.org/10.1038/s41467-020-20102-6.

Patzner, M.S., Logan, M., McKenna, A.M., Young, R.B., Zhou, Z., Joss, H., Mueller, C.W., Hoeschen, C., Scholten, T., Straub, D., Kleindienst, S., Borch, T., Kappler, A., Bryce, C., 2022. Microbial iron cycling during palsa hillslope collapse promotes greenhouse gas emissions before complete permafrost thaw. Commun. Earth Environ. 3 (1), 76. https://doi.org/10.1038/s43247-022-00407-8.

Payandi-Rolland, D., Shirokova, L.S., Tesfa, M., Bénézeth, P., Lim, A.G., Kuzmina, D., Karlsson, J., Giesler, R., Pokrovsky, O.S., 2020. Dissolved organic matter biodegradation along a hydrological continuum in permafrost peatlands. Sci. Total Environ. 749, 141463 https://doi.org/10.1016/j.scitotenv.2020.141463.

Pedersen, J.A., Simpson, M.A., Bockheim, J.G., Kumar, K., 2011. Characterization of soil organic carbon in drained thaw-lake basins of Arctic Alaska using NMR and FTIR photoacoustic spectroscopy. Org. Geochem. 42 (8), 947–954. https://doi.org/10.1016/j.orggeochem.2011.04.003.

Picard, A., Gartman, A., Cosmidis, J., Obst, M., Vidoudez, C., Clarke, D.R., Girguis, P.R., 2019. Authigenic metastable iron sulfide minerals preserve microbial organic carbon in anoxic environments. Chem. Geol. 530, 119343 https://doi.org/10.1016/j.chemgeo.2019.119343.

Pienitz, R., Doran, P.T., Lamoureux, S.F., 2008. Origin and geomorphology of lakes in the polar regions. In: Polar Lakes and Rivers: Limnology of Arctic and Antarctic Aquatic Ecosystems, pp. 25–41. https://doi.org/10.1093/acprof:oso/9780199213887.003.0002.

Pokrovsky, O.S., Manasypov, R.M., Loiko, S.V., Krickov, I.A., Kopysov, S.G., Kolesnichenko, L.G., Vorobyev, S.N., Kirpotin, S.N., 2016. Trace element transport in western Siberian rivers across a permafrost gradient. Biogeosciences 13 (6), 1877–1900. https://doi.org/10.5194/bg-13-1877-2016.

Pokrovsky, O.S., Karlsson, J., Giesler, R., 2018. Freeze-thaw cycles of Arctic thaw ponds remove colloidal metals and generate low-molecular-weight organic matter. Biogeochemistry 137 (3), 321–336. https://doi.org/10.1007/s10533-018-0421-6.

Ravel, B., Newville, M., 2005. ATHENA, ARTEMIS, HEPHAESTUS: data analysis for X-ray absorption spectroscopy using IFEFFIT. J. Synchrotron Radiat. 12 (4), 537–541. https://doi.org/10.1107/S0909049505012719.

Scharlemann, J.P.W., Tanner, E.V.J., Hiederer, R., Kapos, V., 2014. Global soil carbon: understanding and managing the largest terrestrial carbon pool. Carb. Manage. 5 (1), 81–91. https://doi.org/10.4155/cmt.13.77.

Schindelin, J., Arganda-Carreras, I., Frise, E., Kaynig, V., Longair, M., Pietzsch, T., Preibisch, S., Rueden, C., Saalfeld, S., Schmid, B., Tinevez, J.Y., 2012. Fiji: an open-source platform for biological-image analysis. Nat. Methods 9 (7), 676–682. https://doi.org/10.1038/nmeth.2019.

Schuur, E.A.G., McGuire, A.D., Schädel, C., Grosse, G., Harden, J.W., Hayes, D.J., Hugelius, G., Koven, C.D., Kuhry, P., Lawrence, D.M., Natali, S.M., Olefeldt, D., Romanovsky, V.E., Schaefer, K., Turetsky, M.R., Treat, C.C., Vonk, J.E., 2015. Climate change and the permafrost carbon feedback. Nature 520 (7546), 171–179. https://doi.org/10.1038/nature14338.

Sidhu, P.S., Gilkes, R.J., Cornell, R.M., Posner, A.M., Quirk, J.P., 1981. Dissolution of iron oxides and oxyhydroxides in hydrochloric and perchloric acids. Clays Clay Miner. 29 (4), 269–276. https://doi.org/10.1346/CCMN.1981.0290404.

Stookey, L.L., 1970. Ferrozine—a new spectrophotometric reagent for iron. Anal. Chem. 42 (7), 779–781. https://doi.org/10.1021/ac60289a016.

Stubičan, V., Roy, R., 1961. Infrared spectra of layer-structure silicates. J. Am. Ceram. Soc. 44 (12), 625–627. https://doi.org/10.1111/j.1151-2916.1961.tb11670.x.

Tamocai, C., Canadell, J.G., Schuur, E.A.G., Kuhry, P., Mazhitova, G., Zimov, S., 2009. Soil organic carbon pools in the northern circumpolar permafrost region. Global Biogeochem. Cycles 23 (2). https://doi.org/10.1029/2008GB003327.

Tang, J., Yurova, A.Y., Schurgers, G., Miller, P.A., Olin, S., Smith, B., Siewert, M.B., Olefeldt, D., Pilesjö, P., Poska, A., 2018. Drivers of dissolved organic carbon export in a subarctic catchment: importance of microbial decomposition, sorption-desorption, peatland and lateral flow. Sci. Total Environ. 622–623, 260–274. https://doi.org/10.1016/j.scitotenv.2017.11.252.

ThomasArrigo, L.K., Mikutta, C., Byrne, J., Barmettler, K., Kappler, A., Kretzschmar, R., 2014. Iron and arsenic speciation and distribution in organic flocs from streambeds of an arsenic-enriched peatland. Environ. Sci. Tech. 48 (22), 13218–13228. https://doi.org/10.1021/es503550g.

ThomasArrigo, L.K., Notini, L., Shuster, J., Nydegger, T., Vontobel, S., Fischer, S., Kappler, A., Kretzschmar, R., 2022. Mineral characterization and composition of Fe-rich flocs from wetlands of Iceland: implications for Fe, C and trace element export. Sci. Total Environ. 816, 151567 https://doi.org/10.1016/j.scitotenv.2021.151567.

Turetsky, M.R., Abbott, B.W., Jones, M.C., Anthony, K.W., Olefeldt, D., Schuur, E.A.G., Grosse, G., Kuhry, P., Hugelius, G., Koven, C., Lawrence, D.M., Gibson, C., Sannel, A. B.K., McGuire, A.D., 2020. Carbon release through abrupt permafrost thaw. Nat. Geosci. 13 (2), 138–143. https://doi.org/10.1038/s41561-019-0526-0.

Van Bodegom, P.M., Scholten, J.C., Stams, A.J., 2004. Direct inhibition of methanogenesis by ferric iron. FEMS Microbiol. Ecol. 49 (2), 261–268. https://doi.org/10.1016/j.femsec.2004.03.017.

Vonk, J.E., Tank, S.E., Bowden, W.B., Laurion, I., Vincent, W.F., Alekseychik, P., Amyot, M., Billet, M.F., Canário, J., Cory, R.M., Deshpande, B.N., Helbig, M., Jammet, M., Karlsson, J., Larouche, J., MacMillan, G., Rautio, M., Walter Anthony, K.M., Wickland, K.P., 2015. Reviews and syntheses: effects of permafrost thaw on Arctic aquatic ecosystems. Biogeosciences 12 (23), 7129–7167. https://doi.org/10.5194/bg-12-7129-2015.

Vonk, J.E., Tank, S.E., Walvoord, M.A., 2019. Integrating hydrology and biogeochemistry across frozen landscapes. Nat. Commun. 10 (1), 5377. https://doi.org/10.1038/s41467-019-13361-5.

Walch, H., von der Kammer, F., Hofmann, T., 2022. Freshwater suspended particulate matter—key components and processes in floc formation and dynamics. Water Res. 220, 118655 https://doi.org/10.1016/j.watres.2022.118655.

Walter Anthony, K., Schneider von Deimling, T., Nitze, I., Frolking, S., Emond, A., Daanen, R., Anthony, P., Lindgren, P., Jones, B., Grosse, G., 2018. 21st-century modeled permafrost carbon emissions accelerated by abrupt thaw beneath lakes. Nat. Commun. 9 (1), 3262. https://doi.org/10.1038/s41467-018-05738-9.

Xiao, Y.H., Hoikkala, L., Kasurinen, V., Tiirola, M., Kortelainen, P., Vähätalo, A.V., 2016. The effect of iron on the biodegradation of natural dissolved organic matter. J. Geophys. Res. Biogeo. 121 (10), 2544–2561. https://doi.org/10.1002/2016JG003394.

Zeitvogel, F., Schmid, G., Hao, L., Ingino, P., Obst, M., 2016. ScatterJ: an ImageJ plugin for the evaluation of analytical microscopy datasets. J. Microsc. 261 (2), 148–156. https://doi.org/10.1111/jmi.12187.